







# Computationally Efficient MPC for Modular Multilevel Matrix Converters Operating With Fixed Switching Frequency

RODRIGO H. CUZMAR <sup>1,2</sup>, ANDRÉS MORA <sup>3</sup> (Member, IEEE), JAVIER PEREDA <sup>1</sup> (Senior Member, IEEE),  
RICARDO P. AGUILERA <sup>2</sup> (Member, IEEE), PABLO POBLETE <sup>1,2</sup> (Member, IEEE),  
AND SEBASTIÁN NEIRA <sup>1,4</sup> (Student Member, IEEE)

<sup>1</sup>Department of Electrical Engineering and the UC Energy Research Center, Pontificia Universidad Católica de Chile, Santiago 7820436, Chile

<sup>2</sup>School of Electrical and Data Engineering, University of Technology Sydney, Broadway, NSW 2007, Australia

<sup>3</sup>Department of Electrical Engineering, Universidad Técnica Federico Santa María, Valparaíso 2390123, Chile

<sup>4</sup>Institute for Energy Systems, School of Engineering, University of Edinburgh, EH8 9YL Edinburgh, U.K.

CORRESPONDING AUTHOR: JAVIER PEREDA (e-mail: jepereda@uc.cl).

This work was supported in part by ANID projects, with funding prioritized in terms of contribution, including Fondecyt/1220928, FONDAP/1522A0006 SERC Chile, Fondecyt/1231030, Fondecyt/1231030, Fondecyt/1231030, Fondecyt/1231030, and Basal Project FB0008 Advanced Center for Electrical and Electronic Engineering; and in part by the Australian Government through the Australian Research Council (Discovery Project DP210101382). The work of R. H. Cuzmar was supported by the ANID under Grant ANID/AnidNacional/21200622.

**ABSTRACT** Modular multilevel matrix converters stand out for their performance in ac–ac high-power conversion. However, they require multiple control loops to govern the currents from both ac ports, the internal circulating currents, and the capacitor voltages. This article proposes a computationally efficient model predictive control (MPC) strategy based on a new converter modeling to exploit the phase-shifted pulsewidth modulation working principle fully, achieving four improvements: 1) control unification of both ac-ports currents, circulating currents, and capacitor voltages; 2) constrained optimization to safeguard the converter limits; 3) computational burden reduction and high scalability compared to standard MPC strategies; and 4) wide frequency operation with fast closed-loop transient responses, low harmonic distortion, and fixed switching frequency.

**INDEX TERMS** Direct ac-to-ac conversion, model predictive control (MPC), modular multilevel matrix converter (M3C), phase shifted pulsewidth modulation (PS-PWM), sequential analysis, triple-star bridge cells (TSBC).

## I. INTRODUCTION

Modular multilevel cascaded converters (MMCCs) are considered the next generation technology for medium and high power applications given by its high quality voltage waveform, modularity, and capability to directly connect at medium and high voltages [1], [2], [3], [4], [5]. The cascaded H-bridge (CHB), the modular multilevel converter (M2C), the modular multilevel matrix converter (M3C), and Hexverter are some examples of MMCCs.

In terms of ac to ac power conversion, the back-to-back M2C (B2B-MMC) and the M3C are the preferred power converters to use for applications such as, wind energy conversion systems (WECS) and medium/high voltage motor drives for

marine propulsion, mills, pumps, conveyors, power system interconnections (50–60 Hz), and low frequency ac (LFAC) transmission systems [6].

The M3C, also known as triple-star bridge cell (TSBC) converter, has been compared with B2B-M2C for ac-ac applications [6]. As a result, in comparison with the B2B-M2C, the M3C directly performed ac-to-ac conversion without a high voltage dc-link [4], [5], and needs less submodules (SMs) [7]. Moreover, for low frequencies and high power applications, such as LFAC transmission systems, WECS and low speed motor drives, the M3C has shown a better performance [6]. Nevertheless, the implementation of the M3C has been hampered due to its control complexity, dealing with a highly

coupled system, several floating capacitors, a big number of control signals, and critical operating frequencies [8], [9].

A standard approach to solve the previously mentioned challenges is considering a several proportional-integral (PI) or proportional-resonant (PR) controllers [4], [5], [7], [8], [10]. However, the robustness of the closed-loop response is reduced when using multiple single-input-single output (SISO) controllers in highly coupled systems with more variable than degrees of freedom in comparison with multiple-inputs–multiple-outputs (MIMO) controllers. Additionally, the tuning of linear controllers works for a local operating point, outside this region the multiple SISO strategy performance worsens.

The finite-control-set model-predictive-control (FCS-MPC) has been proposed in the literature to solve the aforementioned SISO control limitations [11], [12], [13]. However, the FCS-MPC introduces other disadvantages, such as a spread frequency spectrum, mainly concentrated at low frequencies, due to the lack of a modulation stage, and requires a high computational effort, which increases exponentially with the number of SMs, limiting the implementation of FCS-MPC to M3Cs with a reduced number of SMs. In [14], a continuous-control-set MPC (CCS-MPC) has been proposed in the literature, but that strategy is designed to only control the circulating currents. In [15], [16], and [17], the MPC strategies have been designed to balance the energy among clusters generating the optimal circulating currents. Nonetheless, these strategies do not govern the currents or balance the energy among SMs of the M3C. In [18], an MPC strategy is proposed to balance the energy among SMs in a cluster, achieving a faster dynamic response in comparison with a standard algorithm for phase-shifted pulsewidth modulation (PS-PWM). Nevertheless, this approach do not perform the current control of the M3C. To account for these drawbacks, a sequential PS-MPC has been proposed for multilevel converters to improve the frequency spectrum and reduce the computational burden of the MPC. The PS-MPC exploits the sequential working principle of a PS-PWM, which allows the MPC to only optimize the duty-cycle of the switch that is going to be updated next. The PS-MPC was initially implemented in a single-phase flying capacitor converter [19], and then proposed to govern a CHB converter with independent power SMs [20], and an M2C in order to include multiple control objectives (ac current, circulating currents, and capacitor voltages balance) [21]. Nevertheless, in [19], [20], and [21], the optimal unconstrained solution of the control inputs are saturated and might not be the optimal during transients.

This article proposes a remodeling of the M3C for the design and implementation of a tailor-made sequential PS-MPC, which considers the coupling of the states, the control input constraints, and simplifies the control structure in comparison with multiple-SISO-based control strategies. Thus, the proposed control strategy is formulated to control the cluster currents directly in the double  $\alpha\beta 0$  framework and the SM capacitor voltages by only computing nine control signals at

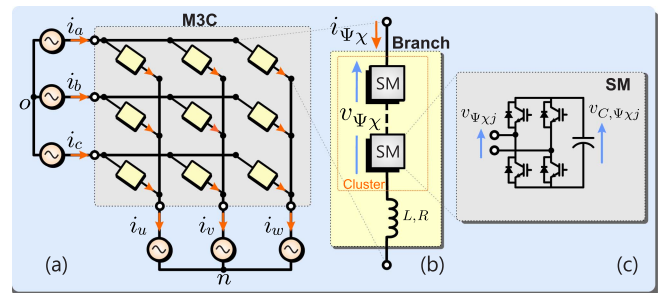


**FIGURE 1. M3C topology: (a) circuit diagram; (b)  $N$ -cell cluster; and (c) full-bridge-based SM.**

each sampling instant independently of the number of SMs of the converter. This increases the scalability and applicability in comparison with a standard FCS-MPC. In addition, the proposed strategy directly considers the dynamic of the three-phase ac-ports, allowing to include different types of loads in the optimal control problem.

The contribution and novelty of this article is the reformulation of the M3C modeling to apply a computationally efficient MPC strategy that fully exploits the working principle of the PS-PWM technique, including the dynamic particularities of this MMCC topology. Furthermore, in contrast to previous PS-MPC strategies, this work achieves the optimal solution not only in steady-state, but also during transients.

Therefore, the M3C model was formulated to achieve a decoupled set of current equations, while maintaining the control input in the original framework when they need to be constrained for a safe converter operation. In addition, the M3C has a very particular dynamic at different operating frequencies, which was considered by the proposed model. Therefore, the contribution of this work is not the simple application of the sequential PS-MPC to an M3C but rather the remodeling of the converter and algorithm to achieve the following advantages: 1) a unified control structure to control the SM capacitor voltages and the arm currents considering the control input limits as bound constraints; 2) reduced computational burden by computing only one control signal per cluster at each sampling time; 3) scalability to operate with a large number of SMs; and 4) fast closed-loop transient response with low distortion and capability to track multiple frequency wave-forms in the arm currents.

Experimental results are provided to verify the proposal performance and effectiveness, showing a fast dynamic response, a low harmonic distortion, and a suitable computational burden operating with a single centralized controller.

## II. M3C MODEL

The M3C topology is composed of nine stacks or clusters to interconnect two three-phase ac-ports [see Fig. 1(a)]. Each cluster is formed by connecting several H-bridges cells or SMs in cascade manner along with a series cluster inductor [see Fig. 1(b)]. In addition, as shown in Fig. 1(c), each SM has a floating capacitor in its dc-link.

The M3C has four control targets: the currents of both ac-ports; the circulating currents; and the capacitor voltages of each SM. The balancing of the capacitor voltages can be indirectly attained by implementing three energy control strategies [14], [17], [22]: 1) *Total Energy Balancing (TEB) Control*: Regulate the energy stored in all capacitors to the desired level by transferring power to or from the ac ports. 2) *Intercluster Balancing (ICB) Control*: Distributes the power of the M3C among all its clusters, determining the imposition of internal command signals for the common-mode voltage and the circulating currents, without affecting the ac ports. However, the ICB should generate minimal circulating currents to increase the efficiency and power density of the converter. 3) *Local-Cluster Balancing (LCB) Control*: Locally regulates the capacitor voltage of each SM in each cluster. It is usually implemented at the modulation stage. In addition, when the converter operates at a shallow frequency in any external port, but most acutely when these frequencies get closer or equal, it is necessary to mitigate large oscillations in the SM capacitor voltages by injecting a proper CMV and additional circulating current components. The latter control task is referred to as low-frequency oscillation (LFO) mitigation.

#### A. MODELLING OF THE M3C

Considering the circuit diagram of the M3C shown in Fig. 1(a), the continuous-time model of each branch current,  $i_{\Psi\chi}$ , can be expressed via

$$\frac{d}{dt}i_{\Psi\chi} = \frac{1}{L}(v_{\Psi} - ri_{\Psi\chi} - v_{\Psi\chi} - v_{\chi} - v_{\text{no}}) \quad (1)$$

where  $\Psi \in \{a, b, c\}$  and  $\chi \in \{u, v, w\}$ . Here,  $L$  and  $r$  are the inductance and the resistance of the cluster filter, respectively. Additionally, the variables  $v_{\Psi}$  and  $v_{\chi}$  stand for the input and the output-port voltage in each phase, respectively; and  $v_{\text{no}}$  denotes voltage between the neutral points. The cluster voltage,  $v_{\Psi\chi}$ , is formed by the sum of all its individual SM voltages, i.e.,

$$v_{\Psi\chi} = \sum_{j=1}^N v_{\Psi\chi j}. \quad (2)$$

In (2),  $v_{\Psi\chi j}$  is the  $j$ th SM output voltage and its average value over a switching period is given by

$$v_{\Psi\chi j} = v_{C,\Psi\chi j} \delta_{\Psi\chi j} \quad (3)$$

where  $\delta_{\Psi\chi j}(t) \in \mathbb{D} \triangleq [-1, 1]$  represents the duty cycle of the  $j$ th SM in the  $\Psi\chi$ -cluster, which is the control input of the system. Moreover, the dynamic model of each capacitor voltage,  $v_{C,\Psi\chi j}$ , is given by

$$\frac{d}{dt}v_{C,\Psi\chi j} = \frac{1}{C}i_{\Psi\chi} \delta_{\Psi\chi j} \quad (4)$$

Then, by applying the above equations to all nine arms, the following dynamic model for the cluster currents is obtained:

$$L \frac{d}{dt} \begin{bmatrix} i_{\text{au}} & i_{\text{bu}} & i_{\text{cu}} \\ i_{\text{av}} & i_{\text{bv}} & i_{\text{cv}} \\ i_{\text{aw}} & i_{\text{bw}} & i_{\text{cw}} \end{bmatrix} = \begin{bmatrix} v_a & v_b & v_c \\ v_a & v_b & v_c \\ v_a & v_b & v_c \end{bmatrix} - r \begin{bmatrix} i_{\text{au}} & i_{\text{bu}} & i_{\text{cu}} \\ i_{\text{av}} & i_{\text{bv}} & i_{\text{cv}} \\ i_{\text{aw}} & i_{\text{bw}} & i_{\text{cw}} \end{bmatrix} - \begin{bmatrix} v_{\text{au}} & v_{\text{bu}} & v_{\text{cu}} \\ v_{\text{av}} & v_{\text{bv}} & v_{\text{cv}} \\ v_{\text{aw}} & v_{\text{bw}} & v_{\text{cw}} \end{bmatrix} - \begin{bmatrix} v_u & v_u & v_u \\ v_v & v_v & v_v \\ v_w & v_w & v_w \end{bmatrix} - v_{\text{no}} \begin{bmatrix} 1 & 1 & 1 \\ 1 & 1 & 1 \\ 1 & 1 & 1 \end{bmatrix}. \quad (5)$$

The cluster currents presented in (5) have input, output, and circulating currents mixed. To facilitate the control design, the so-called  $\alpha\beta 0$  transformation is applied to (5) in order to obtain decoupled currents. The  $\alpha\beta 0$  transformation matrix is given by

$$\mathbf{C}^{\alpha\beta 0} = \sqrt{\frac{2}{3}} \begin{bmatrix} 1 & -\frac{1}{2} & -\frac{1}{2} \\ 0 & \frac{\sqrt{3}}{2} & -\frac{\sqrt{3}}{2} \\ \frac{1}{\sqrt{2}} & \frac{1}{\sqrt{2}} & \frac{1}{\sqrt{2}} \end{bmatrix} = \begin{bmatrix} c_1^{\alpha} & c_2^{\alpha} & c_3^{\alpha} \\ c_1^{\beta} & c_2^{\beta} & c_3^{\beta} \\ c_1^0 & c_2^0 & c_3^0 \end{bmatrix} = \begin{bmatrix} \mathbf{C}^{\alpha} \\ \mathbf{C}^{\beta} \\ \mathbf{C}^0 \end{bmatrix}. \quad (6)$$

The M3C model can be represented in the double- $\alpha\beta 0$ -framework ( $\text{D-}\alpha\beta 0$ ) premultiplying by  $[\mathbf{C}^{\alpha\beta 0}]$  and postmultiplying by  $[\mathbf{C}^{\alpha\beta 0}]^T$ , resulting in the following decoupled model:

$$L \frac{d}{dt} \begin{bmatrix} i_{\alpha\alpha} & i_{\beta\alpha} & i_{0\alpha} \\ i_{\alpha\beta} & i_{\beta\beta} & i_{0\beta} \\ i_{\alpha 0} & i_{\beta 0} & 0 \end{bmatrix} = \sqrt{3} \begin{bmatrix} 0 & 0 & 0 \\ 0 & 0 & 0 \\ v_{\Psi}^{\alpha} & v_{\Psi}^{\beta} & 0 \end{bmatrix} - r \begin{bmatrix} i_{\alpha\alpha} & i_{\beta\alpha} & i_{0\alpha} \\ i_{\alpha\beta} & i_{\beta\beta} & i_{0\beta} \\ i_{\alpha 0} & i_{\beta 0} & 0 \end{bmatrix} - \begin{bmatrix} v_{\alpha\alpha} & v_{\beta\alpha} & v_{0\alpha} \\ v_{\alpha\beta} & v_{\beta\beta} & v_{0\beta} \\ v_{\alpha 0} & v_{\beta 0} & v_{00} \end{bmatrix} - \sqrt{3} \begin{bmatrix} 0 & 0 & v_{\chi}^{\alpha} \\ 0 & 0 & v_{\chi}^{\beta} \\ 0 & 0 & 0 \end{bmatrix} - \begin{bmatrix} 0 & 0 & 0 \\ 0 & 0 & 0 \\ 0 & 0 & 3v_{\text{no}} \end{bmatrix}. \quad (7)$$

The double- $\alpha\beta 0$  representation allows to directly govern input, output, and circulating currents of the converter because they are fully decoupled [4], [5], [8], [22]. Thus, the dynamic of the both three-phase systems can be directly considered in the model, e.g., a three-phase inductive load

$$\begin{bmatrix} v_{\chi}^{\alpha} \\ v_{\chi}^{\beta} \\ v_{\chi} \end{bmatrix} = r_L \begin{bmatrix} i_{\chi}^{\alpha} \\ i_{\chi}^{\beta} \\ i_{\chi} \end{bmatrix} + L_L \frac{d}{dt} \begin{bmatrix} i_{\chi}^{\alpha} \\ i_{\chi}^{\beta} \\ i_{\chi} \end{bmatrix} \quad (8)$$

where  $L_L$  and  $r_L$  are the inductance and the resistance of the load, respectively. Moreover, the relation between the  $\alpha\beta 0$   $uvw$ -current and the  $\text{D-}\alpha\beta 0$  cluster current is given by

$$\begin{bmatrix} i_{\chi}^{\alpha} \\ i_{\chi}^{\beta} \\ i_{\chi} \end{bmatrix} = \sqrt{3} \begin{bmatrix} i_{0\alpha} \\ i_{0\beta} \end{bmatrix}. \quad (9)$$

**TABLE 1. System Variables**

Variable	Definition	Description
$\mathbf{i}^{\alpha\beta 0}(k)$	$\begin{bmatrix} i_{\alpha\alpha} & i_{\alpha\beta} & i_{\alpha 0} & i_{\beta\alpha} & i_{\beta\beta} & i_{\beta 0} & i_{0\alpha} & i_{0\beta} \end{bmatrix}^T$	D- $\alpha\beta 0$ cluster current vector
$\mathbf{v}_{C,j}(k)$	$\begin{bmatrix} v_{C,aj}^T(k) & v_{C,bj}^T(k) & v_{C,cj}^T(k) \end{bmatrix}^T$	Capacitor voltage $j$ vector
$\mathbf{v}_{C,\Psi_j}(k)$	$\begin{bmatrix} v_{C,\Psi_{uj}}(k) & v_{C,\Psi_{vj}}(k) & v_{C,\Psi_{wj}}(k) \end{bmatrix}^T$	Capacitor voltage $\Psi_j$ vector
$\delta_j(k)$	$\begin{bmatrix} \delta_{aj}^T(k) & \delta_{bj}^T(k) & \delta_{cj}^T(k) \end{bmatrix}^T$	Control signal $j$ vector
$\delta_{\Psi_j}(k)$	$\begin{bmatrix} \delta_{\Psi_{uj}}(k) & \delta_{\Psi_{vj}}(k) & \delta_{\Psi_{wj}}(k) \end{bmatrix}^T$	Control signal $\Psi_j$ vector

Thus, the dynamic of the  $abc$ -port can be directly considered as function of the D- $\alpha\beta 0$  cluster currents

$$\begin{bmatrix} v_{\chi}^{\alpha} \\ v_{\chi}^{\beta} \\ v_{\chi}^0 \end{bmatrix} = \sqrt{3}r_L \begin{bmatrix} i_{0\alpha} \\ i_{0\beta} \end{bmatrix} + \sqrt{3}L_L \frac{d}{dt} \begin{bmatrix} i_{0\alpha} \\ i_{0\beta} \end{bmatrix}. \quad (10)$$

### B. DISCRETE-TIME MODEL

This work formulates the PS-MPC strategy for an M3C to control the transformed cluster currents and to perform the LCB control in a simple and unified manner. For that purpose, the system state, at each instant  $k$ , is chosen as

$$\mathbf{x}(k) = \begin{bmatrix} \mathbf{i}^{\alpha\beta 0T}(k) & \mathbf{v}_{C,1}^T(k) & \dots & \mathbf{v}_{C,N}^T(k) \end{bmatrix}^T \in \mathbb{R}^{8+9N} \quad (11)$$

where  $\mathbf{i}^{\alpha\beta 0}(k) \in \mathbb{R}^8$  is the current vector in the double- $\alpha\beta 0$  framework and  $\mathbf{v}_{C,j}(k) \in \mathbb{R}^9$  is the vector comprising the capacitor voltage of the  $j$ -SM of each cluster. Moreover, the control input vector,  $\mathbf{u}(k)$ , is defined by

$$\mathbf{u}(k) = \begin{bmatrix} \delta_1^T(k) & \dots & \delta_N^T(k) \end{bmatrix}^T \in \mathbb{D}^{9N} \quad (12)$$

where  $\delta_j(k)$  comprises the modulating signals arranged analogously as the capacitor voltage vector. The vectors in (11) and (12) are summarized in Table 1.

Additionally, the three-phase systems voltages at the input ( $abc$ -port) and output ( $uvw$ -port) of the converter in the  $\alpha\beta 0$ -framework are defined as

$$\begin{aligned} \mathbf{v}_{\Psi}^{\alpha\beta}(k) &= \begin{bmatrix} v_{\Psi}^{\alpha}(k) & v_{\Psi}^{\beta}(k) \end{bmatrix}^T \\ \mathbf{v}_{\chi}^{\alpha\beta}(k) &= \sqrt{3}r_L \begin{bmatrix} i_{0\alpha} \\ i_{0\beta} \end{bmatrix} + \sqrt{3}L_L \frac{d}{dt} \begin{bmatrix} i_{0\alpha} \\ i_{0\beta} \end{bmatrix}. \end{aligned} \quad (13)$$

Finally, by considering (11)–(13) and applying the forward Euler discretization to (4) and (7) using a sampling period  $T_s$ , the following discrete-time model can be obtained:

$$\mathbf{x}(k+1) = \mathbf{A}\mathbf{x}(k) + \mathbf{B}(\mathbf{x}(k))\mathbf{u}(k) + \mathbf{E}_{\Psi}\mathbf{v}_{\Psi}^{\alpha\beta}(k) \quad (14)$$

where

$$\begin{aligned} \mathbf{A} &= \begin{bmatrix} \mathbf{A}^{\text{up}} & \mathbf{0}_{8 \times 9N} \\ \mathbf{0}_{9N \times 8} & \mathbf{I}_{9N} \end{bmatrix}, \quad \mathbf{E}_{\Psi} = \sqrt{3} \frac{T_s}{L} \begin{bmatrix} \mathbf{0}_{2 \times 2} \\ 1 & 0 \\ \mathbf{0}_{2 \times 2} \\ 0 & 1 \\ \mathbf{0}_{2+9N \times 2} \end{bmatrix} \\ \mathbf{B}(\mathbf{x}(k)) &= \begin{bmatrix} \mathbf{B}_1^{\text{up}}(\mathbf{x}_k) & \mathbf{B}_2^{\text{up}}(\mathbf{x}_k) & \dots & \mathbf{B}_N^{\text{up}}(\mathbf{x}_k) \\ \mathbf{B}_1^{\text{lo}}(\mathbf{x}_k) & \mathbf{0}_{9 \times 9} & \dots & \mathbf{0}_{9 \times 9} \\ \mathbf{0}_{9 \times 9} & \mathbf{B}_2^{\text{lo}}(\mathbf{x}_k) & \ddots & \vdots \\ \vdots & \ddots & \ddots & \mathbf{0}_{9 \times 9} \\ \mathbf{0}_{9 \times 9} & \dots & \mathbf{0}_{9 \times 9} & \mathbf{B}_N^{\text{lo}}(\mathbf{x}_k) \end{bmatrix} \end{aligned} \quad (15)$$

with  $\mathbf{x}_k := \mathbf{x}(k)$ . This model arrangement will be exploited in the following section to design the proposed sequential PS-MPC control strategy.

### III. PS-MPC OF AN M3C

This section formulates the proposed PS-MPC to directly govern the cluster currents in the double- $\alpha\beta 0$  framework and to balance the SM capacitor voltages in a unified and computation efficient manner. This formulation is not straightforward and is one of the contributions of this work.

#### A. OVERALL OPTIMAL CONTROL PROBLEM

The main control targets are to balance the SMs capacitor voltages, and to track the desired references for input, output, and circulating currents of the M3C, which can be expressed via

$$\mathbf{x}^*(k) = \begin{bmatrix} \mathbf{i}^{\alpha\beta 0*T}(k) & \mathbf{v}_{C,1}^T(k) & \dots & \mathbf{v}_{C,N}^T(k) \end{bmatrix}^T. \quad (16)$$

In order to tackle this multivariable closed-loop objective, the standard quadratic cost function is used

$$J(k) = \|\mathbf{x}(k+1) - \mathbf{x}^*(k+1)\|_{\mathbf{Q}}^2 + \|\mathbf{u}(k) - \mathbf{u}^*(k)\|_{\Lambda}^2 \quad (17)$$

where  $\mathbf{u}^*(k)$  is the required steady-state control input to keep the SMs capacitor voltages and the transformed cluster currents in the desired steady-state  $\mathbf{x}^*(k+1)$  as per (16). The diagonal matrix  $\Lambda = \lambda \mathbf{I}_{9N}$  is used to adjust the compromise between the state tracking error and the control effort, allowing the dynamic response of the closed-loop system to be modified [23]. Moreover, the weighting matrix  $\mathbf{Q} = \text{diag}\{\sigma_1 \mathbf{I}_8, \sigma_2 \mathbf{I}_{9N}\}$  regulates the tracking error of the SMs capacitor voltages versus the cluster currents in the D- $\alpha\beta 0$  framework.

#### B. SEQUENTIAL AVERAGE MODEL OF AN M3C

This work considers the working principle of a PS-PWM to formulate a sequential PS-MPC for the M3C. For this converter,  $N$  carriers are phase shifted by  $\pi/N$ . In addition, in a digital implementation, the control signals  $\delta_{auj}$ ,  $\delta_{avj}$ ,  $\delta_{awj}$ ,  $\delta_{bu j}$ ,  $\delta_{bvj}$ ,  $\delta_{bwj}$ ,  $\delta_{cu j}$ ,  $\delta_{cvj}$ , and  $\delta_{cwj}$  are updated when its associated carrier  $v_{cr,j}$  is at one of its edges (PS-PWM with

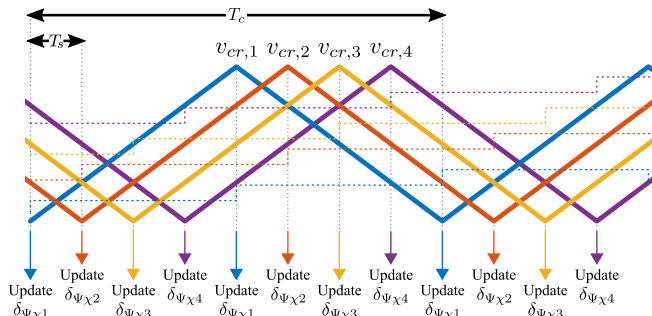


**FIGURE 2.** PS-PWM operating principle in double update mode for a four-SM arm.

double update). After that, these signals remain constant until the next update, which is after half of the carrier period ( $T_c/2$ ). This leads to a sequential control signal update process as illustrated in Fig. 2 for  $N = 4$  SMs. Notice that only nine modulating control signals (one SM per cluster) need to be obtained at each sampling instant,  $T_s = T_c/(2N)$ . If single-update is considered for the PS-PWM, the duty cycles are updated at the top or the bottom edges only, so the sampling time changes when updating the last SM to  $(N + 1)T_c/(2N)$ . Because of these asymmetrical sampling times, the single-update of the PS-PWM is not commonly used for arms based on H-bridges.

Based on the double update operation of the modulator, it is possible to derive a sequential model of the M3C from (14) by considering at each sampling instant only the “actives” control signals  $\delta_j$  (the ones that needs to be updated) as control input as follows:

$$\mathbf{u}_j(k) = \delta_j(k) \in \mathbb{D}^9 \quad (18)$$

and the sequential state vector as

$$\mathbf{x}_j(k) = \left[ \mathbf{i}^{\alpha\beta 0^T}(k) \quad \mathbf{v}_{C,j}^T(k) \right]^T \in \mathbb{R}^{17}. \quad (19)$$

Consequently, the dynamic model (14) can be rewritten as

$$\mathbf{x}_j(k+1) = \mathbf{A}_j \mathbf{x}_j(k) + \mathbf{B}_j \mathbf{u}_j(k) + \mathbf{h}_j(k) \quad (20)$$

with

$$\mathbf{h}_j(k) = \mathbf{E}_{\psi,j} \mathbf{v}_{\psi}^{\alpha\beta}(k) + \sum_{\substack{l=1 \\ l \neq j}}^N \begin{bmatrix} \mathbf{B}_l^{\text{up}} \\ \mathbf{0}_{9 \times 9} \end{bmatrix} \mathbf{u}_l(k) \quad (21)$$

where  $\mathbf{u}_l$  contains the “inactive” control signals that have been previously obtained. Therefore,  $\mathbf{h}_j(k)$  can be seen as a known disturbance for the sequential average model and the

sequential state, input and grid matrices are

$$\mathbf{A}_j = \begin{bmatrix} \mathbf{A}^{\text{up}} & \mathbf{0}_{8 \times 9} \\ \mathbf{0}_{9 \times 8} & \mathbf{I}_9 \end{bmatrix} \in \mathbb{R}^{17 \times 17}, \quad \mathbf{E}_{\psi,j} = \frac{T_s}{L} \begin{bmatrix} \mathbf{0}_{2 \times 2} & \sqrt{3} & 0 \\ \mathbf{0}_{2 \times 2} & 0 & \sqrt{3} \\ \mathbf{0}_{11 \times 2} \end{bmatrix} \in \mathbb{R}^{17 \times 2} \quad (22)$$

$$\mathbf{B}_j(\mathbf{x}_j(k)) = \begin{bmatrix} \mathbf{B}_j^{\text{up}}(\mathbf{x}_j(k)) \\ \mathbf{B}_j^{\text{lo}}(\mathbf{x}_j(k)) \end{bmatrix} \in \mathbb{R}^{17 \times 9}.$$

### C. SEQUENTIAL OPTIMAL CONTROL PROBLEM

By adopting the sequential average model in (20), the cost function (17) can be reduced taking into account only the active control signals, leading to the following sequential cost function:

$$J_j(k) = \|\mathbf{x}_j(k+1) - \mathbf{x}_j^*(k+1)\|_{\mathbf{Q}_j}^2 + \|\mathbf{u}_j(k) - \mathbf{u}_j^*(k)\|_{\Lambda_j}^2 \quad (23)$$

with

$$\mathbf{Q}_j = \text{diag} \{ \sigma_1 \mathbf{I}_8, \sigma_2 \mathbf{I}_9 \} \in \mathbb{R}^{17 \times 17} \text{ and } \Lambda_j = \lambda \mathbf{I}_9 \in \mathbb{R}^{9 \times 9}. \quad (24)$$

Therefore, the optimal PS-PWM active control signals are those that minimize this sequential cost function, i.e.,

$$\begin{aligned} \mathbf{u}_j^{\text{opt}}(k) &= \arg \min_{\mathbf{u}_j(k)} \{ J_j(k) \} \\ \text{s.t. } & -\mathbf{1}_{9 \times 1} \leq \mathbf{u}_j(k) \leq \mathbf{1}_{9 \times 1}. \end{aligned} \quad (25)$$

Notice that (25) is in fact a box-constrained quadratic programming problem, since  $\mathbf{u}_j(k) \in \mathbb{D}^9 \triangleq [-1, 1]^9 \subset \mathbb{R}^9$ . In contrast to previous PS-MPC strategies reported in the literature (e.g., [19], [20], [21]), in which suboptimal solutions are obtained by using the saturated version of the unconstrained solution of (25), this work uses an exterior point active set method based on a Lagrangian function and the Karush–Kuhn–Tucker conditions to compute optimal duty cycles to be applied by the converter. For further details on the algorithm used in this work, we refer readers to [24]. The proposed optimal approach impacts the system’s performance, especially during transients, as will be analyzed in the experimental validation of the proposed control strategy.

### IV. REFERENCES DESIGN

The overall control strategy is shown in Fig. 3. This section aims to obtain the state references,  $\mathbf{x}_j^*(k)$ , and the steady-state reference,  $\delta_j^*$ . Considering current of both ports, TEB and ICB controls

$$\mathbf{x}_j^*(k) = \left[ \mathbf{i}^{\alpha\beta 0^*T}(k) \quad \mathbf{v}_{C,j}^{*T}(k) \right]^T \in \mathbb{R}^{17} \quad (26)$$

where each element of  $\mathbf{v}_{C,j}^*(k)$  is considered constant and equal to  $v_{\text{dc}}^*$ . In addition, the steady-state control inputs  $\mathbf{u}_j^*(k) = \delta_j^*(k) \in \mathbb{D}^9$  are also determined in this section.

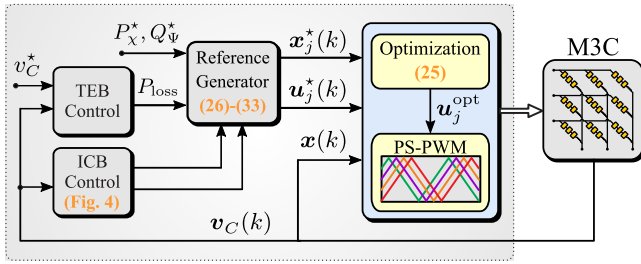


FIGURE 3. Overall control scheme.

### A. INPUT AND OUTPUT CURRENT REFERENCE

The references for input and output currents are designed in the  $\alpha\beta 0$ -framework. By considering an active power references for the output system, a symmetric current reference is obtained

$$i_{\chi}^{\alpha\beta} = \sqrt{\frac{P_{\chi}^*}{r_L}} \begin{bmatrix} \sin(\omega_{\chi} t) \\ -\cos(\omega_{\chi} t) \end{bmatrix} \quad (27)$$

where  $P_{\chi}^*$  is the active power reference. Then, in order to regulate the average energy of the converter (TEB control), the required input active power  $P_{\chi}^*$  must be the sum of the desired output active power  $P_{\Psi}^*$  and the power consumed by the M3C,  $P_{\text{loss}}$ . This leads to the following expression for the input current reference:

$$i_{\Psi}^{\alpha\beta} = \frac{1}{v_{\Psi}^{\alpha 2} + v_{\Psi}^{\beta 2}} \begin{bmatrix} v_{\Psi}^{\alpha} & v_{\Psi}^{\beta} \\ v_{\Psi}^{\beta} & -v_{\Psi}^{\alpha} \end{bmatrix} \begin{bmatrix} P_{\chi}^* + P_{\text{loss}} \\ Q_{\Psi}^* \end{bmatrix}. \quad (28)$$

The power losses  $P_{\text{loss}}$  are obtained by the TEB control, which is composed by a PI controller as is shown in Fig. 3, that allows to regulate the internal energy of the converter by considering the tracking error of the sum of the capacitor voltage references and the sum of the capacitor voltage measurements.

Finally, the current references in the  $D-\alpha\beta 0$  framework for both ports are given by

$$\begin{bmatrix} i_{\alpha 0}^* \\ i_{\beta 0}^* \\ i_{0\alpha}^* \\ i_{0\beta}^* \end{bmatrix} = \frac{1}{\sqrt{3}} \begin{bmatrix} i_{\Psi}^{\alpha\beta} \\ i_{\chi}^{\alpha\beta} \end{bmatrix}. \quad (29)$$

### B. CIRCULATING CURRENT REFERENCE

The ICB control considers the energy balance among clusters, designing a proper circulating current. By analyzing the cluster powers and cluster voltages in the  $D-\alpha\beta 0$ -framework the waveform for the circulating current can be deduced as presented in [4], [5], [22]. In this work, the ICB control introduced in [4] is implemented. Where the circulating currents are given by the sum of positive and negative sequence in phase with the input-port; and the amplitudes  $I_{d1}^*$ ,  $I_{d2}^*$ ,  $I_{d3}^*$ ,  $I_{d4}^*$ ,  $I_{d5}^*$ ,  $I_{d6}^*$ ,  $I_{q1}^*$ , and  $I_{q2}^*$  are obtained by PI controllers in order to regulate the cluster imbalance in the  $D-\alpha\beta 0$ -framework as shows Fig. 4.

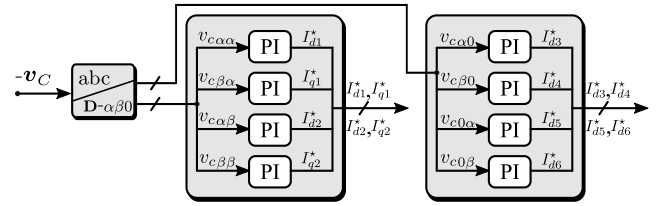


FIGURE 4. Inter-cluster balancing control proposed in [4].

### C. MODULATION INDEX REFERENCE

The modulation index references for each arm is key to obtain a good steady-state performance and a reduced current spectra under the PS-MPC scheme. These references are generated by considering the system in the desired steady-state, i.e.,  $i^{\alpha\beta 0}(k) = i^{\alpha\beta 0*}(k)$ . Thus, by substituting the current references into the dynamic model (7), it is possible to calculate the desired steady-state voltages in the  $\alpha\beta 0$ -framework as

$$\begin{bmatrix} v_{\alpha\alpha}^* & v_{\beta\alpha}^* & v_{0\alpha}^* \\ v_{\alpha\beta}^* & v_{\beta\beta}^* & v_{0\beta}^* \\ v_{\alpha 0}^* & v_{\beta 0}^* & v_{00}^* \end{bmatrix} = \sqrt{3} \begin{bmatrix} 0 & 0 & 0 \\ 0 & 0 & 0 \\ v_{\Psi}^{\alpha} & v_{\Psi}^{\beta} & 0 \end{bmatrix} - L \frac{d}{dt} \begin{bmatrix} i_{\alpha\alpha}^* & i_{\beta\alpha}^* & i_{0\alpha}^* \\ i_{\alpha\beta}^* & i_{\beta\beta}^* & i_{0\beta}^* \\ i_{\alpha 0}^* & i_{\beta 0}^* & 0 \end{bmatrix} \\ - \begin{bmatrix} i_{\alpha\alpha}^* & i_{\beta\alpha}^* & i_{0\alpha}^* \\ i_{\alpha\beta}^* & i_{\beta\beta}^* & i_{0\beta}^* \\ i_{\alpha 0}^* & i_{\beta 0}^* & 0 \end{bmatrix} - \sqrt{3} \begin{bmatrix} 0 & 0 & v_{\chi}^{\alpha} \\ 0 & 0 & v_{\chi}^{\beta} \\ 0 & 0 & 0 \end{bmatrix} - \begin{bmatrix} 0 & 0 & 0 \\ 0 & 0 & 0 \\ 0 & 0 & 3v_{\text{no}} \end{bmatrix}. \quad (30)$$

Then, by premultiplying by  $[\mathbf{C}^{\alpha\beta 0}]^T$  and postmultiplying by  $[\mathbf{C}^{\alpha\beta 0}]$ , the voltages obtained in (30) can be represented in the original framework

$$\begin{bmatrix} v_{au}^* & v_{bu}^* & v_{cu}^* \\ v_{av}^* & v_{bv}^* & v_{cv}^* \\ v_{aw}^* & v_{bw}^* & v_{cw}^* \end{bmatrix} = [\mathbf{C}^{\alpha\beta 0}]^T \begin{bmatrix} v_{\alpha\alpha}^* & v_{\beta\alpha}^* & v_{0\alpha}^* \\ v_{\alpha\beta}^* & v_{\beta\beta}^* & v_{0\beta}^* \\ v_{\alpha 0}^* & v_{\beta 0}^* & v_{00}^* \end{bmatrix} [\mathbf{C}^{\alpha\beta 0}]. \quad (31)$$

Thus, the modulation index is obtained by dividing the desired ac cluster voltage  $v_{\Psi\chi}^*$  by the available cluster capacitor voltage

$$\delta_{\Psi\chi j}^* = \frac{v_{\Psi\chi}^*}{\sum_{l=1}^N v_{C,\Psi\chi l}}. \quad (32)$$

Finally, the input reference  $u_j^*$  required by the proposed controller in (23) is obtained by arranging multiple modulation indexes as

$$\delta_j^* = \begin{bmatrix} \delta_{auj}^* & \delta_{avj}^* & \delta_{awj}^* & \delta_{buj}^* & \delta_{bvj}^* & \delta_{bwj}^* & \delta_{cuj}^* & \delta_{cvj}^* & \delta_{cwj}^* \end{bmatrix}^T. \quad (33)$$

### V. CONTROL STRATEGIES COMPARISON

Simulation results have been performed to compare the proposed sequential PS-MPC strategy performance with existing strategies when governing an M3C connected to a three-phase

**TABLE 2.** System Parameters for Comparison

Variable	Description	Comparison
$P$	Rated power	3 kW
$v_{\Psi}$	Input grid voltage (line-to-line rms)	190 V
$f_{\Psi}$	Input grid frequency	60 Hz
$r_L$	Output resistance	14 $\Omega$
$L_L$	Output inductance	1 mH
$f_{\chi}$	Output frequency	50 Hz
$N$	SMs per clusters	4
$C$	SM capacitance	987 $\mu\text{F}$
$v_{dc}^*$	dc cap. voltage per SM	100 V
$L$	Cluster filter inductance	5 mH
$r$	Cluster filter resistance	0.1 $\Omega$
$f_{cr}$	Carrier frequency	1 kHz

system and a passive load. The parameters used for simulations are presented in Table 2.

Two strategies have been considered to compare the proposal, the first control strategy is the standard PI strategy for the current and LCB control presented in [4], [5], [8], [9] and a reduced FCS-MPC strategy [25]. The PI strategy considers four PIs controllers to control the input and output currents in two  $dq$ -frameworks, four proportional ( $P$ ) controllers to govern the circulating currents and 36  $P$  controllers to achieve the balance among SMs. The second control strategy is based on a FCS-MPC strategy [25]. The FCS-MPC considers the feasible SM output voltage, so for a four-SM M3C converter the total states are  $3^{9N} = 3^{36} \approx 1.5 \times 10^{17}$ , which cannot be implemented in a simulation environment, even less in a real application. However, the total combinations can be reduced by considering the common-mode voltage as a known disturbance. Therefore, the total combinations are reduced to  $9 \times 3^N = 9 \times 3^4 = 729$ , making its implementation feasible, at least in simulation. Nonetheless, the computational burden of this predictive strategy increases exponentially with the number of SMs of the converter. As the common-mode voltage is considered as a known disturbance, each cluster is decoupled in terms of control objectives of the others. In terms of control structure, the proposed PS-MPC and FCS-MPC strategies present a simpler structure than the PI strategy, reducing from four PIs and 40 Ps SISO controllers to one MIMO controller. The tuning process of the predictive strategies is heuristic, considering standard steps. Regarding the PI controllers, the tuning was made in order to obtain a second-order close-loop response with a natural frequency of 150 Hz and a damping factor of 0.7071 and the LCB proportional controllers were tuned with a gain of 0.1.

The comparison of the three strategies is shown in Figs. 5 and 6. In steady-state, all the strategies achieve the references, obtaining balanced input and output currents, and balanced clusters and SMs with a mean capacitor voltage equal to 100 V as present Fig. 5(a)–(c). However, the proposal achieves a mix of advantages from the other two strategies, such as, fast

dynamic and tracking error response, low harmonic distortion, and scalability.

### 1) POWER STEP CHANGE

The comparison in terms of input and output currents are presented in Fig. 5(a) and (b). In term of the settling time, the dynamic response of the predictive strategies is considerably faster than the PI strategy. The response of the FCS-MPC and PS-MPC is practically instantaneous, in contrast, the PI strategy achieves the input and output current reference after 60 and 25 ms, respectively.

### 2) CIRCULATING CURRENT TRACKING

The circulating current tracking error for the PI strategy is bounded by  $\pm 15$  A. Nevertheless, the tracking error for the predictive strategies is lower than 5 A, where he FCS-MPC achieves the best performance [see Fig. 5(d)].

### 3) CLUSTER VOLTAGES

The  $au$ -cluster voltage and its spectrum are presented in Fig. 5(e) and (f), respectively. The FCS-MPC strategy generates a disperse spectrum around 8 kHz as it does not have a modulator. On the other hand, the PS-MPC and PI strategies generate a spectrum centered on 8 kHz and its multiples, which comes from the PS-PWM with 1 kHz carriers ( $f_{o,sw} = 2Nf_{cr} = 8$  kHz). The PI strategy generates the highest cluster voltage THD (15.16%), while the FCS-MPC strategy has the lowest THD (13.74%). In addition, the FCS-MPC strategy has the highest weighted total harmonic distortion (WTHD = 1.75%), and the PI strategy has the lowest WTHD (0.12%). In summary, the proposal considerably reduces the WTHD (73% lower than the FCS-MPC), achieving a lower input and output current ripple than the FCS-MPC [see Fig. 5(a) and (b)], and limiting the frequency spectrum to a band determined by the PS-PWM.

### 4) LOCAL-CLUSTER BALANCING CONTROL

The performance of the LCB control is shown in Fig. 6. At the beginning, the capacitor voltage references of the  $au$ -cluster are set for different values, while maintaining its average voltage of 100 V. At the instant  $t = 100$  ms, the references for all capacitor voltages are set to 100 V. The FCS-MPC strategy achieves the fastest dynamic response ( $t = 110$  ms), followed by the proposed PS-MPC ( $t = 180$  ms), and far behind is the classical PI strategy ( $t = 475$  ms). The PI strategy adjusts the duty cycle per SM using a proportional controller before the modulation stage. When the duty cycle saturates, its control action is limited. Unlike the PI, which considers two stages to control currents and balance capacitors, the PS-MPC controls currents and balances capacitors in a single stage. The formulated PS-MPC optimizes each duty cycle, adjusting the duty cycle to balance the voltage of the SMs by considering not only the tracking error of capacitor voltages, but the tracking error of the current and steady-state duty cycle reference. Therefore, the boundary of the SM balancing control depends

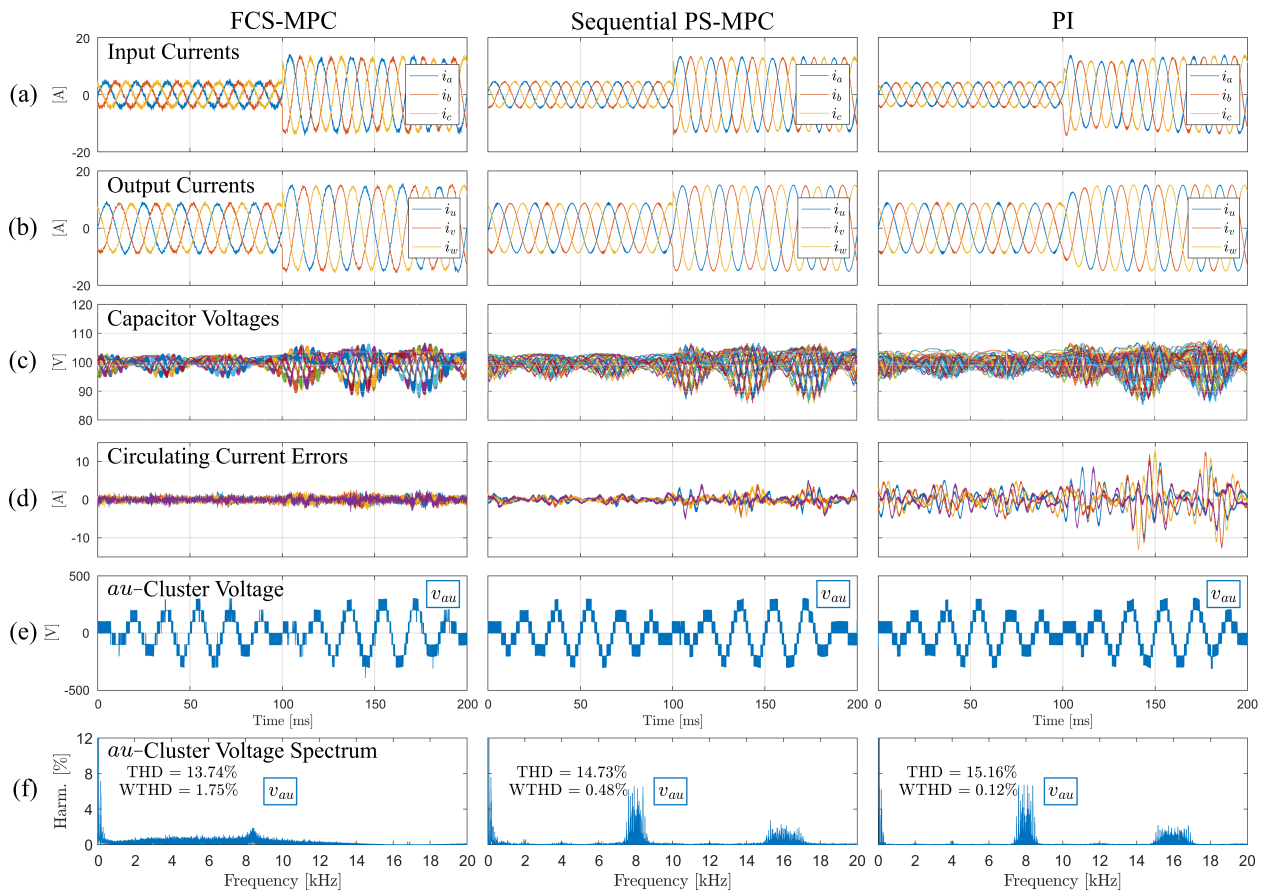


**FIGURE 5.** Simulation comparison, FCS-MPC strategy (left), the proposed sequential PS-MPC strategy (middle) and PI in  $dq$ -framework strategy proposed in [4] (right). (a) Input currents, (b) output currents, (c) capacitor voltages, (d) circulating currents tracking error, (e)  $au$ -cluster voltage, and (f)  $au$ -cluster voltage spectra.

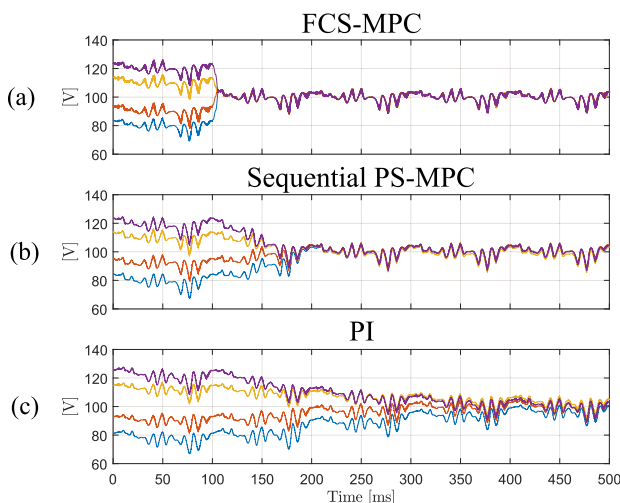


**FIGURE 6.** Comparison under local-cluster imbalance. Capacitor voltages of  $au$ -cluster with (a) FCS-MPC strategy, (b) sequential PS-MPC proposed strategy, and (c) PI strategy.

on the tracking errors, the control effort and the weighting factors.

Table 3 summarizes the comparison among the control strategies. The proposed sequential PS-MPC, against the standard PI strategy, presents a faster dynamic response, a better cluster current, and voltage tracking. The proposal overcomes the FCS-MPC with a lower WTHD and a fixed frequency spectrum. Moreover, unlike the FCS-MPC, the computational burden does not depend of the number of SMs, the predictive model considers the coupling among clusters and a lower average SM switching frequency. In terms of average tracking error, the best strategy is the reduced FCS-MPC with a current and voltage error of 0.48 A and 2.03 V, the worst strategy is the PI with a current and voltage error of 1.57 A and 2.59 V. So, the performance of the proposed sequential PS-MPC is a balance between the PI and FCS-MPC strategies. The differences between the predictive strategies and the PI strategy, in terms of tracking error, is given by capability to track multiple-frequency waveforms that the predictive strategies have.

Finally, it is important to emphasise that even though FCS-MPC might offer some benefits when compared to the proposed PS-MPC (e.g., fast capacitor voltage balancing), its disadvantages are substantial: 1) it has a dispersed frequency spectrum that complicates the design of reactors and filters, in addition to producing random switching losses and low-order



**TABLE 3.** Comparison Among the Proposed and Existing Control Methods in Steady-State At 3 Kw ( $N = 4$ )

	PI [4]	FCS-MPC	Proposed
Controller	Multiple PI Loops	Reduced FCS-MPC	Sequential PS-MPC
Cluster coupling consideration	No	No	Yes
Average current tracking error	16.02 %	4.13 %	8.55 %
Average voltage tracking error	2.59 %	2.03 %	2.18 %
Average SM switching frequency	2 kHz	3.6 kHz	2 kHz
Input/output current quality	Very good	Fair (noisy)	Very Good
Input/output current response	Slow	Fast	Fast
Capacitor voltage balance	Slow	Very fast	Fast
Circulating current tracking error	High peaks	Noisy with very low peaks	Noiseless with low peaks
Output voltage THD	15.16%	13.74%	14.73%
Output voltage WTHD	0.12%	1.75%	0.48%
Output voltage spectrum	Fixed at 8 and 16 kHz	Spread at low frequencies (<12 kHz)	Fixed at 8 and 16 kHz
Modulation	PS-PWM (1 kHz)	None	PS-PWM (1 kHz)
Sample time	125 [ $\mu$ s]	*60 [ $\mu$ s]	125 [ $\mu$ s]
Scalability effort	Low	High (exponentially with N)	Low

\*The sampling time was adjusted in order to obtain an average switching frequency of 8 kHz.

harmonics (it has the highest WTHD) (see Fig. 5); 2) it has the highest average SM switching frequency, leading to a higher power losses than the other strategies (see Table 3); and 3) it has a high computational cost that cannot be implemented when the number of SMs increases (see Section VI-C).

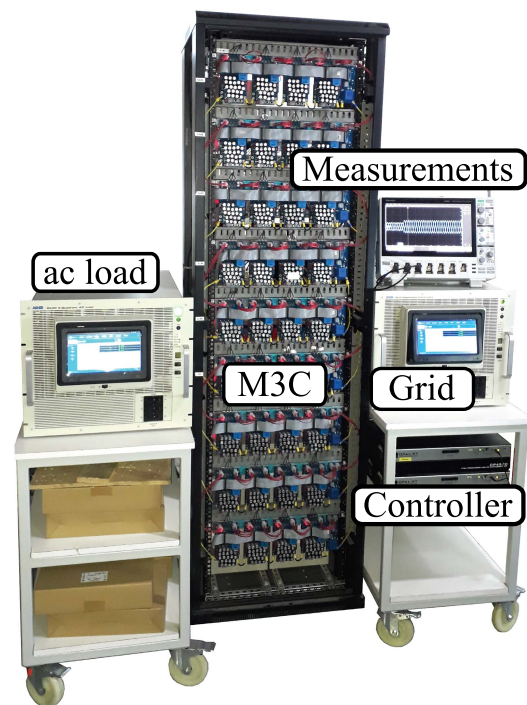
These are where the benefits of the proposed PS-MPC can be appreciated, as will be experimentally validated in the following Section.

## VI. EXPERIMENTAL RESULTS

Experimental results have been performed to analyze and verify the proposed sequential PS-MPC strategy performance when governing an M3C connected to a three-phase system and a passive load. The grid-voltage of the first system was generated by a grid-simulator NHR9410 and the passive load of the second was generated by a regenerative ac load NHR9430. The predictive control scheme was implemented on an OPAL-RT OP4510 system. The data are acquired by the OPAL-RT software every 62.5  $\mu$ s and is not postprocessed. The prototype is presented in Fig. 7 and the main setup parameters are summarized in Table 4. The proposed PS-MPC generates an apparent output switching frequency of  $f_{o,sw} = 2Nf_{cr} = 16$  kHz. However, since a double update mode is considered, it results in a sampling frequency of  $f_s = 32$  kHz. In addition, the PS-MPC was tuned heuristically with  $\sigma_1 = 1$ ,  $\sigma_2 = 0.2$  and  $\lambda = 20$  [19], [20], and the execution time is  $T_e = 7.5 \mu$ s.

### A. STEADY-STATE PERFORMANCE.

The results of the closed-loop steady-state performance are presented in the left side of Fig. 8. The sequential PS-MPC is able to properly govern the M3C, achieving a symmetric waveform for the input and the output currents as shown Fig. 8(a) and (b). Additionally, in Fig. 8(c), the control strategy successfully regulates the capacitor voltages, keeping them around the reference of 150 V. Moreover, the circulating currents are properly tracked in order to balance the converter clusters and reduce the capacitor voltage ripple. It is important

**FIGURE 7.** 3 kVA experimental prototype.

to mention that this control strategy is able to track any current waveform, including several frequencies in comparison with other control strategies that uses proportional controllers [4], [5], [8], [9]. This can be seen in Fig. 8(d), where the circulating currents are tracked and they present more than one frequency (references are presented behind in gray).

### B. DYNAMIC PERFORMANCE

The results of the closed-loop dynamic response performance are presented in the middle and right side of the Fig. 8. The middle part of Fig. 8 corresponds to the dynamic response of

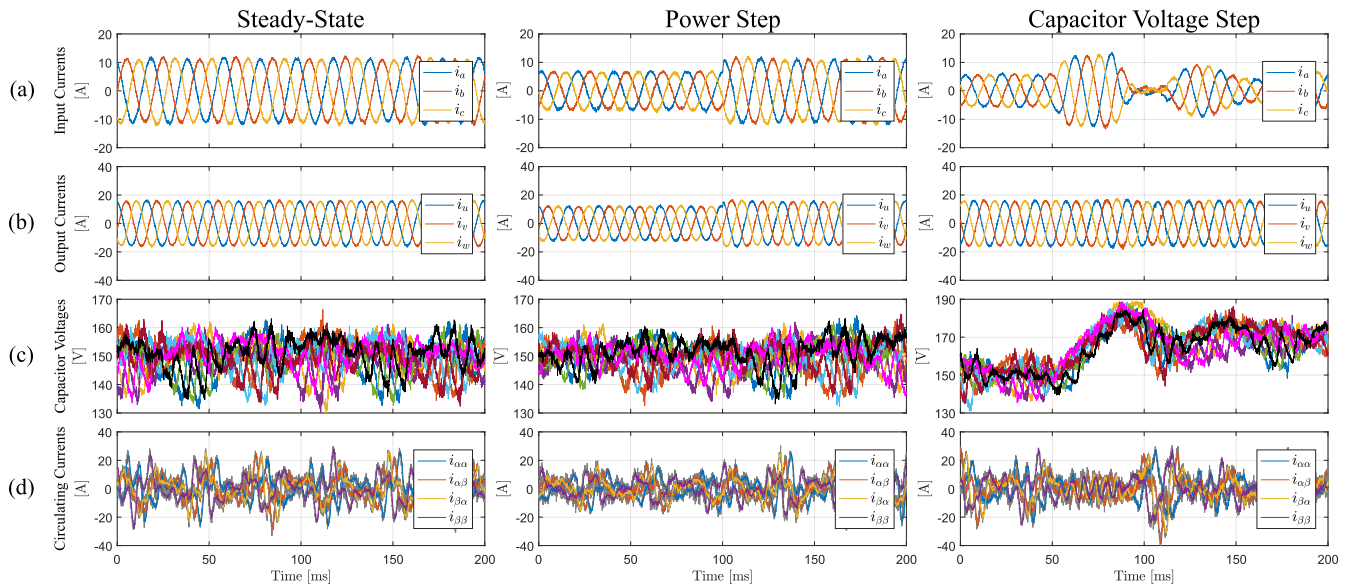


**FIGURE 8.** Experimental steady-state performance (left), dynamic response performance under a sudden power change (middle) and dynamic response under a sudden capacitor voltage change (right). (a) Input currents, (b) output currents, (c) capacitor voltages, and (d) circulating current.

**TABLE 4.** System Parameters for Experimental Results

Variable	Description	Fig. 8 / Other
$P$	Rated power	5 / 3 kW
$v_{\Psi}$	Input grid voltage (line-to-line rms)	380 / 190 V
$f_{\Psi}$	Input grid frequency	50 / 60 Hz
$r_L$	Output resistance	14 $\Omega$
$L_L$	Output inductance	1 mH
$f_{\chi}$	Output frequency	60 / 10-59 Hz
$N$	SMs per clusters	4
$C$	SM capacitance	987 $\mu\text{F}$
$v_{dc}^*$	dc cap. voltage per SM	150 / 100 V
$L$	Cluster filter inductance	5 mH
$r$	Cluster filter resistance	0.1 $\Omega$
$f_{cr}$	Carrier frequency	2 kHz

the control strategy under a step change in the power transferred from the input- to the output-port from 3 to 5 kW and the right side is the dynamic response under a step change in the capacitor voltage reference of each SM from 150 to 170 V.

### 1) POWER STEP CHANGE

The dynamic response, in terms of a suddenly power change, is almost instantaneous and does not present overshoot. The peak value of the input and output currents increase due to the power step and the speed of the change is fast as it is shown in Fig. 8(a) and (b). In Fig. 8(c), the ripple of the capacitor voltages augment because the power step, nevertheless, the mean value of the capacitor remains constant. Finally, the circulating currents increase their peak values proportional to the change of the power and, despite the step change, the tracking error is properly followed as Fig. 8(d) shows.

### 2) CAPACITOR VOLTAGE STEP CHANGE

The results of the dynamic response under a step change in the capacitor voltages are presented in the right side of Fig. 8. In terms of capacitor voltage, the dynamic response is mainly given by the outer PI controller, since this PI regulates the inner energy of the converter, which is directly related with the capacitor voltages and this behavior can be seen in Fig. 8(c). In addition, the input current in Fig. 8(a) is directly affected by the outer PI controller because this creates the reference,  $P_{\text{loss}}$ , that is used for the reference of the input currents. Nonetheless, the output current is not directly affected by the outer PI, the speed of the stabilization is mainly given by the sequential PS-MPC as is shown in Fig. 8(b). Finally, the circulating current reference, in Fig. 8(d) are slightly reduced due to the increment of the capacitor voltage reference. This occurs because the system is still exchanging the same energy from input to output and the relation between the energy and the capacitor voltage is quadratic.

### 3) DIFFERENT OUTPUT FREQUENCIES PERFORMANCE

The proposed strategy allows to govern the M3C for different output frequencies, Fig. 9 shows experimental results for three different output frequencies (50, 10, and 59 Hz, respectively). The illustrated measurements are the phase-*a* current, the phase-*u* current, the *au*-cluster current, and the output voltage of *au*-cluster with its frequency domain. The output current is achieved independent of the frequency. Moreover, the converter is able to operate close to critical points (0 and 60 Hz). Mitigation currents must be considered in order to achieve critical points; however, this is not the scope of this proposal. Considering a carrier frequency of 2 kHz and a PS-PWM modulation, the output voltage spectrum is centered at 16 kHz, this behavior occurs for the three cases. The phase-*a* input current presents a THD of 2.29% and a WTHD of 0.59%.

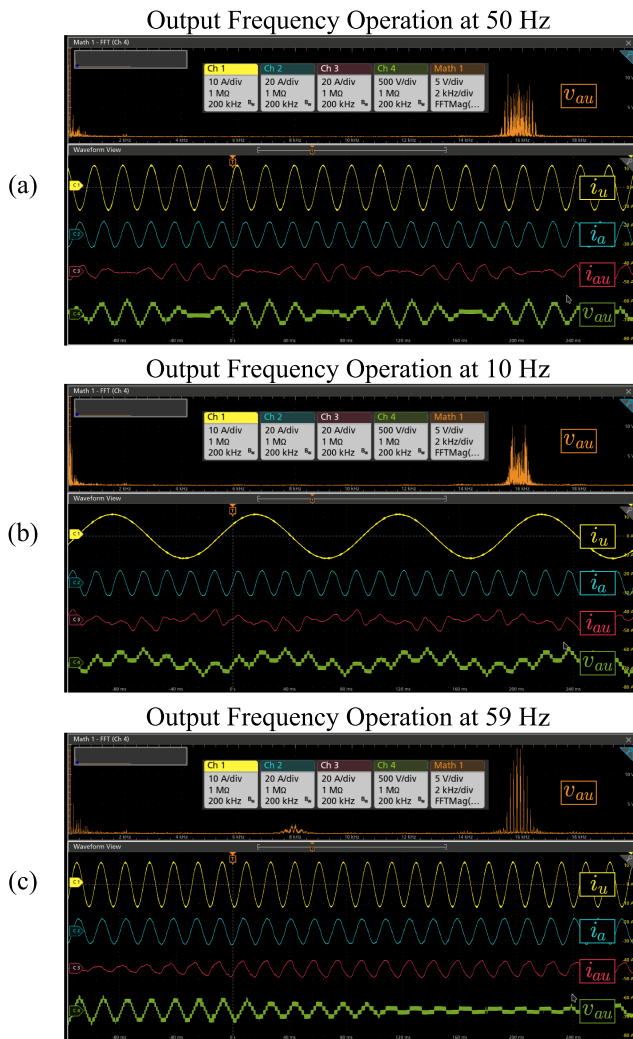


**FIGURE 9.** Experimental steady-state performance. (Ch 1) output current  $u$ , (Ch 2) input current  $a$ , (Ch 3) current  $au$ -cluster, (Ch 4) output voltage  $au$ -cluster, and (Math 1) output voltage  $au$ -cluster spectrum. (a) Output frequency at 50 Hz, (b) output frequency at 10 Hz, and (c) output frequency at 59 Hz.

On the other hand, the phase- $u$  output current has a lower THD and WTHD, which are 0.79% and 0.15%, respectively. These different behaviors between input and output currents, in terms of distortion, is mainly given by the PI controller, which regulates the average energy of the converter because it directly affects the reference generation of the input currents.

#### 4) OPTIMIZATION WITH ACTIVE CONSTRAINTS

The proposal obtains the optimal duty cycles considering upper and lower constraints, this is shown in Fig. 10, where the operating point of the M3C is set in order to force the activation of constraints. The constraints are activated by considering a mean capacitor voltage reference equal to 85 V and forcing a cluster imbalance. The duty cycles generated by the proposed sequential PS-MPC are always optimal, during transient and steady-state, feature that standard control strategies are not able to achieve.

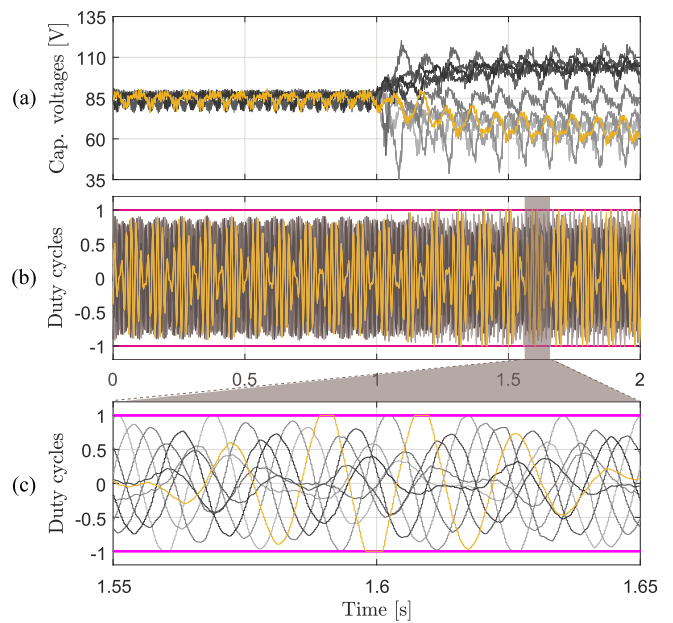


**FIGURE 10.** Experimental constraints activation under an imbalance condition. (a) Capacitor voltages, (b) control signals, and (c) control signals zoom.

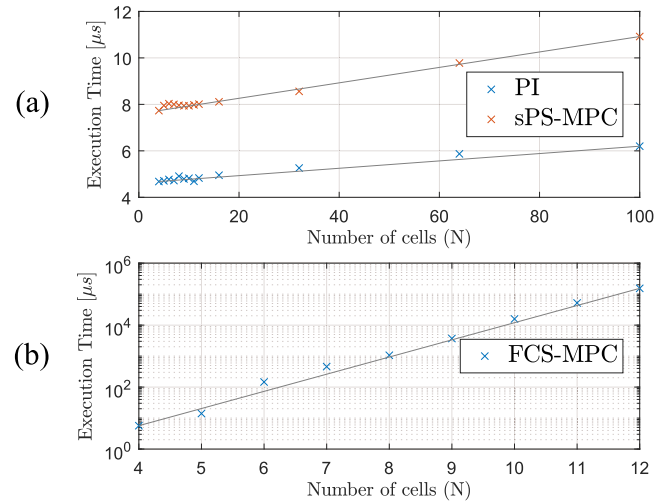


**FIGURE 11.** Experimental execution time control strategies. (a) PI and sequential PS-MPC strategies and (b) FCS-MPC strategy.

#### C. SCALABILITY ANALYSIS OF PS-MPC

The dimension of the optimal problem solved by the sequential PS-MPC is fixed, independently of the number of SMs. By increasing the number of SMs, the expected behavior in the execution time is a linear increment due to each SM contributes to the output voltage, but only one is optimized per sampling time. This linear behavior in the execution time was experimentally proved by the OPAL-RT OP4510. In addition, the computational burden of the PI and FCS-MPC as function of the number of SMs is presented in Fig. 11. The execution time of the sequential PS-MPC and the PI strategies increase linearly with the number of SMs, meanwhile, the increment of the execution time of the FCS-MPC strategy is exponential,

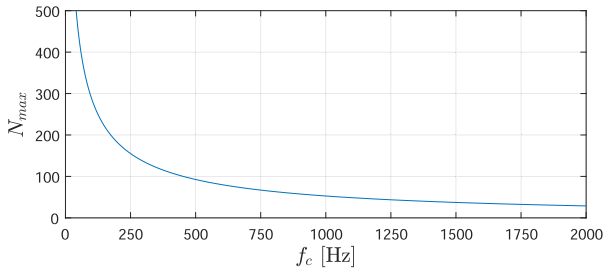


**FIGURE 12.** Maximum number of SMs per carrier frequency that the proposal can handle considering the linear execution time presented in Fig. 11.

limiting the implementation of the FCS-MPC in real-time applications to a reduced number of SMs.

In MMCCs with a large number of SMs for high power and high voltage applications, the carrier frequency should be set as low as possible to reduce the switching losses. The sampling frequency of the proposal is given by  $T_s = 1/(2Nf_c)$ . Therefore, in order to estimate the maximum number of SM per cluster that the proposal can handle as function of the carrier frequency, it is important to determine the execution time as function of  $N$ , which is provided in Fig. 11(a). Finally, by considering the sampling time equal to the execution time  $T_{ex} = T_s = 1/(2Nf_c)$ , the maximum number of SM that the proposal is able to govern as function of the carrier frequency is presented in Fig. 12. It is estimated that the sequential PS-MPC can drive up to 32 SMs per cluster for a carrier frequency of 2 kHz, and up to 249 SMs per cluster when the carrier frequency is reduced to 125 Hz.

## VII. CONCLUSION

This article proposed the formulation and assessment of a sequential PS-MPC strategy to govern an M3C. The proposed controller effectively performs the LCB control task and regulates the input, output, and circulating currents in a single control stage, using an MPC embedded with the load and control input model directly in the optimization. Furthermore, by exploiting the PS-PWM working principle, the proposed PS-MPC method updates, at each sampling instant, only one control signal for every cluster. This significantly reduces the computational burden of the controller, while making it independent of the number of SMs. Therefore, the PS-MPC can be easily scalable to govern M3C with a large number of SMs.

As evidenced by the experimental results, the proposed PS-MPC formulation results in a fast closed-loop dynamic response and effective tracking of the input, output, and circulating currents. In addition, the proposal considers the control input limits in the optimization process and obtains the optimal duty cycles during steady-state and transients. Moreover, the M3C governed by the proposed PS-MPC operates with a fixed switching frequency, low harmonic distortion, and distributed power losses among power switches.

## APPENDIX

### STATE MATRIX COMPONENT OF M3C MODEL

Matrix  $\mathbf{A}^{up}(k)$ , presented in the M3C model (14) and the sequential model (22), is given by

$$\mathbf{A}^{up} = \text{diag} \left\{ \begin{array}{l} 1 - \frac{r}{L} T_s \\ 1 - \frac{r}{L} T_s \\ 1 - \frac{r}{L} T_s \\ 1 - \frac{r}{L} T_s \\ 1 - \frac{r}{L} T_s \\ 1 - \frac{r}{L} T_s \\ 1 - \frac{r_{eq}}{L_{eq}} T_s \\ 1 - \frac{r_{eq}}{L_{eq}} T_s \end{array} \right\} \quad (34)$$

where  $r_{eq} = r + 3r_L$  and  $L_{eq} = L + 3L_L$ .

### INPUT MATRIX COMPONENTS OF M3C MODEL

Matrix  $\mathbf{B}_j^{up}(k)$ , presented in the M3C model (14) and the sequential model (22), is given by

$$\mathbf{B}_j^{up}(k) = -T_s \begin{bmatrix} \frac{1}{L} \mathbf{v}_{C,j}^T(k) \mathbf{M}_{\alpha\alpha} \\ \frac{1}{L} \mathbf{v}_{C,j}^T(k) \mathbf{M}_{\alpha\beta} \\ \frac{1}{L} \mathbf{v}_{C,j}^T(k) \mathbf{M}_{\alpha 0} \\ \frac{1}{L} \mathbf{v}_{C,j}^T(k) \mathbf{M}_{\beta\alpha} \\ \frac{1}{L} \mathbf{v}_{C,j}^T(k) \mathbf{M}_{\beta\beta} \\ \frac{1}{L} \mathbf{v}_{C,j}^T(k) \mathbf{M}_{\beta 0} \\ \frac{1}{L_{eq}} \mathbf{v}_{C,j}^T(k) \mathbf{M}_{0\alpha} \\ \frac{1}{L_{eq}} \mathbf{v}_{C,j}^T(k) \mathbf{M}_{0\beta} \end{bmatrix} \quad (35)$$

where

$$\mathbf{M}_{\alpha\beta} = \begin{bmatrix} c_1^\alpha \text{diag}(\mathbf{C}^\beta) & \mathbf{0}_{3 \times 3} & \mathbf{0}_{3 \times 3} \\ \mathbf{0}_{3 \times 3} & c_2^\alpha \text{diag}(\mathbf{C}^\beta) & \mathbf{0}_{3 \times 3} \\ \mathbf{0}_{3 \times 3} & \mathbf{0}_{3 \times 3} & c_3^\alpha \text{diag}(\mathbf{C}^\beta) \end{bmatrix}. \quad (36)$$

Moreover, matrix  $\mathbf{B}_j^{lo}(k)$  is given by

$$\mathbf{B}_j^{lo}(k) = \frac{T_s}{C} \text{diag} \left\{ \left( \left( \begin{bmatrix} \mathbf{C}^{\alpha\beta 0} & \mathbf{0}_{3 \times 3} & \mathbf{0}_{3 \times 3} \\ \mathbf{0}_{3 \times 3} & \mathbf{C}^{\alpha\beta 0} & \mathbf{0}_{3 \times 3} \\ \mathbf{0}_{3 \times 3} & \mathbf{0}_{3 \times 3} & \mathbf{C}^{\alpha\beta 0} \end{bmatrix}^T \right) \mathbf{T} \right)^2 \begin{bmatrix} i_{\alpha\beta 0}(k) \\ 0 \end{bmatrix} \right\} \quad (37)$$

with

$$\mathbf{T} = \begin{bmatrix} 1 & 0 & 0 & 0 & 0 & 0 & 0 & 0 & 0 \\ 0 & 0 & 0 & 1 & 0 & 0 & 0 & 0 & 0 \\ 0 & 0 & 0 & 0 & 0 & 0 & 1 & 0 & 0 \\ 0 & 1 & 0 & 0 & 0 & 0 & 0 & 0 & 0 \\ 0 & 0 & 0 & 0 & 1 & 0 & 0 & 0 & 0 \\ 0 & 0 & 0 & 0 & 0 & 0 & 0 & 1 & 0 \\ 0 & 0 & 1 & 0 & 0 & 0 & 0 & 0 & 0 \\ 0 & 0 & 0 & 0 & 0 & 1 & 0 & 0 & 0 \\ 0 & 0 & 0 & 0 & 0 & 0 & 0 & 0 & 1 \end{bmatrix}. \quad (38)$$

## REFERENCES

- [1] M. A. Perez, S. Ceballos, G. Konstantinou, J. Pou, and R. P. Aguilera, "Modular multilevel converters: Recent achievements and challenges," *IEEE Open J. Ind. Electron. Soc.*, vol. 2, no. 1, pp. 224–239, Feb. 2021.
- [2] M. A. Perez, S. Bernet, J. Rodriguez, S. Kouro, and R. Lizana, "Circuit topologies, modeling, control schemes, and applications of modular multilevel converters," *IEEE Trans. Power Electron.*, vol. 30, no. 1, pp. 4–17, Jan. 2015.
- [3] F. Briz, M. Lopez, A. Rodriguez, and M. Arias, "Modular power electronic transformers: Modular multilevel converter versus cascaded h-bridge solutions," *IEEE Ind. Electron. Mag.*, vol. 10, no. 4, pp. 6–19, Dec. 2016.
- [4] M. Diaz et al., "Control of wind energy conversion systems based on the modular multilevel matrix converter," *IEEE Trans. Ind. Electron.*, vol. 64, no. 11, pp. 8799–8810, Nov. 2017.
- [5] W. Kawamura, M. Hagiwara, and H. Akagi, "Control and experiment of a modular multilevel cascade converter based on triple-star bridge cells," *IEEE Trans. Ind. Appl.*, vol. 50, no. 5, pp. 3536–3548, Sep./Oct. 2014.
- [6] M. Diaz et al., "An overview of applications of the modular multilevel matrix converter," *Energies*, vol. 13, no. 21, 2020, Art. no. 5546. [Online]. Available: <https://www.mdpi.com/1996-1073/13/21/5546>
- [7] P. Bravo, J. Pereda, M. M. C. Merlin, S. Neira, T. C. Green, and F. Rojas, "Modular multilevel matrix converter as solid state transformer for medium and high voltage AC substations," *IEEE Trans. Power Del.*, vol. 37, no. 6, pp. 5033–5043, Dec. 2022, doi: [10.1109/TPWRD.2022.3166258](https://doi.org/10.1109/TPWRD.2022.3166258).
- [8] M. Diaz et al., "Vector control of a modular multilevel matrix converter operating over the full output-frequency range," *IEEE Trans. Ind. Electron.*, vol. 66, no. 7, pp. 5102–5114, Jul. 2019.
- [9] W. Kawamura, K. Chen, M. Hagiwara, and H. Akagi, "A low-speed, high-torque motor drive using a modular multilevel cascade converter based on triple-star bridge cells (MMCC-TSBC)," *IEEE Trans. Ind. Appl.*, vol. 51, no. 5, pp. 3965–3974, Sep./Oct. 2015.
- [10] J. Ma, M. S. A. Dahidah, V. Pickard, and J. Yu, "A hierarchical energy balance control method for m3c based on injecting output frequency circulating currents," *IEEE Trans. Power Electron.*, vol. 35, no. 3, pp. 2424–2435, Mar. 2020.
- [11] A. Mora, M. Espinoza, M. Diaz, and R. Cardenas, "Model predictive control of modular multilevel matrix converter," in *Proc. IEEE 24th Int. Symp. Ind. Electron.*, 2015, pp. 1074–1079.
- [12] A. Dekka, B. Wu, V. Yaramasu, R. L. Fuentes, and N. R. Zargari, "Model predictive control of high-power modular multilevel converters-an overview," *IEEE Trans. Emerg. Sel. Topics Power Electron.*, vol. 7, no. 1, pp. 168–183, Mar. 2019.
- [13] R. H. Cuzmar, A. Mora, J. Pereda, P. Poblete, and R. P. Aguilera, "Long-horizon sequential FCS-MPC approaches for modular multilevel matrix converters," *IEEE Trans. Ind. Electron.*, vol. 71, no. 5, pp. 5137–5147, May 2024, doi: [10.1109/TIE.2023.3286013](https://doi.org/10.1109/TIE.2023.3286013).
- [14] M. Urrutia, R. Cárdenas, J. Clare, and A. Watson, "Circulating current control for the modular multilevel matrix converter based on model predictive control," *IEEE Trans. Emerg. Sel. Topics Power Electron.*, vol. 9, no. 5, pp. 6069–6085, Oct. 2021.
- [15] B. Fan, K. Wang, P. Wheeler, C. Gu, and Y. Li, "An optimal full frequency control strategy for the modular multilevel matrix converter based on predictive control," *IEEE Trans. Power Electron.*, vol. 33, no. 8, pp. 6608–6621, Aug. 2018, doi: [10.1109/TPEL.2017.2755767](https://doi.org/10.1109/TPEL.2017.2755767).
- [16] M. Urrutia, R. Cárdenas, J. C. Clare, M. Díaz, and A. Watson, "Continuous set model predictive control for energy management of modular multilevel matrix converters," *IEEE Trans. Power Electron.*, vol. 37, no. 5, pp. 5731–5748, May 2022, doi: [10.1109/TPEL.2021.3133695](https://doi.org/10.1109/TPEL.2021.3133695).
- [17] R. Cuzmar, A. Montenegro, A. Mora, J. Pereda, and R. P. Aguilera, "Constrained MPC for intercluster energy control of modular multilevel matrix converters," *IEEE Trans. Ind. Electron.*, to be published, doi: [10.1109/TIE.2023.3303641](https://doi.org/10.1109/TIE.2023.3303641).
- [18] A. Mora et al., "Model-predictive-control-based capacitor voltage balancing strategies for modular multilevel converters," *IEEE Trans. Ind. Electron.*, vol. 66, no. 3, pp. 2432–2443, Mar. 2019, doi: [10.1109/TIE.2018.2844842](https://doi.org/10.1109/TIE.2018.2844842).
- [19] R. P. Aguilera, P. Acuna, X. Su, P. Lezana, and B. McGrath, "Sequential phase-shifted model predictive control for multicell power converters," in *Proc. IEEE Southern Power Electron. Conf.*, 2017, pp. 1–6.
- [20] R. H. Cuzmar, J. Pereda, and R. P. Aguilera, "Phase-shifted model predictive control to achieve power balance of CHB converters for large-scale photovoltaic integration," *IEEE Trans. Ind. Electron.*, vol. 68, no. 10, pp. 9619–9629, Oct. 2020.
- [21] P. Poblete, S. Neira, R. P. Aguilera, J. Pereda, and J. Pou, "Sequential phase-shifted model predictive control for modular multilevel converters," *IEEE Trans. Energy Convers.*, vol. 36, no. 4, pp. 2691–2702, Dec. 2021.
- [22] M. Diaz et al., "An overview of modelling techniques and control strategies for modular multilevel matrix converters," *Energies*, vol. 13, no. 18, 2020, Art. no. 4678. [Online]. Available: <https://www.mdpi.com/1996-1073/13/18/4678>
- [23] R. P. Aguilera and D. E. Quevedo, "Predictive control of power converters: Designs with guaranteed performance," *IEEE Trans. Ind. Informat.*, vol. 11, no. 1, pp. 53–63, Feb. 2015.
- [24] R. Baidya et al., "Enabling multistep model predictive control for transient operation of power converters," *IEEE Open J. Ind. Electron. Soc.*, vol. 1, no. 1, pp. 284–297, Oct. 2020, doi: [10.1109/OJIES.2020.3029358](https://doi.org/10.1109/OJIES.2020.3029358).
- [25] S. Vazquez, J. Rodriguez, M. Rivera, L. G. Franquelo, and M. Norambuena, "Model predictive control for power converters and drives: Advances and trends," *IEEE Trans. Ind. Electron.*, vol. 64, no. 2, pp. 935–947, Feb. 2017.



**RODRIGO H. CUZMAR** received the B.Sc.(Eng.) degree with honors in electrical engineering, in 2017, and the M.Sc. degree in electrical engineering, in 2020, all from Pontificia Universidad Católica de Chile (PUC), Santiago, Chile. He is currently working toward the Ph.D. degree in electrical engineering in a double-degree program with PUC and University of Technology Sydney (UTS), Sydney, NSW, Australia.

Since 2017, he has been part of the Power and Energy Conversion Laboratory (PECLab), PUC.

His current research interests include predictive control of power converters applied to energy storage, solar energy conversion, and industrial applications.



**ANDRÉS MORA** (Member, IEEE) received the B.Sc. and M.Sc. degrees from the Universidad Técnica Federico Santa María (UTFSM), Valparaíso, Chile, in 2007 and 2010, respectively, and the Ph.D. degree from the Universidad de Chile, Santiago, Chile, in 2019, all in electrical engineering.

In 2011, He joined the Electrical Department of the UTFSM, where he is currently an Associate Professor. Since 2023, he has been appointed as an Associate Researcher with the Advanced Center for Electrical and Electronic Engineering (AC3E)

in Chile. His main research interests include advanced control techniques applied to modular multilevel converters, variable speed drives, and microgrids.

Dr. Mora was honored with the IEEE Transactions on Industrial Electronics Best Paper Award in 2019.



**JAVIER PEREDA** (Senior Member, IEEE) received the B.Sc. (Eng.) degree with highest honors in electrical engineering, in 2009, and the M.Sc. and Ph.D. degrees in electrical engineering, in 2013, all from Pontificia Universidad Católica de Chile, Santiago, Chile.

In 2013, he joined the Electrical Department of Pontificia Universidad Católica de Chile, where he is currently an Associate Professor. From 2014 to 2016, he was an Associate Research of the Control and Power Group, Department of Electrical

and Electronic Engineering, Imperial College London. He is an Associate Research of the Solar Energy Research Center, Chile, and the UC Energy Research Center, Chile. He is a Principal Investigator of the Electric Vehicle Laboratory and the Power and Energy Conversion Laboratory (PECLab), Pontificia Universidad Católica de Chile. His research interests include power electronics and control applied to electric vehicles, energy storage, ac and dc electric networks and microgrids, renewable energy, multilevel converters, industrial applications, and motor drives.



**RICARDO P. AGUILERA** (Member, IEEE) received the B.Sc. degree in electrical engineering from the Universidad de Antofagasta, Antofagasta, Chile, the M.Sc. degree in electronics engineering from the Universidad Técnica Federico Santa María, Valparaíso, Chile, and the Ph.D. degree in electrical engineering from The University of Newcastle (UoN), Newcastle, NSW, Australia, in 2003, 2007, and 2012, respectively.

From 2012 to 2013, he was a Research Academic with UoN, where he was part of the Centre for Complex Dynamic Systems and Control. From 2014 to 2016, he was a Senior Research Associate with The University of New South Wales, Australia, where he was part of the Australian Energy Research Institute. Since September 2016, he has been with the School of Electrical and Data Engineering, at the University of Technology Sydney, Australia, where he currently holds an Associate Professor position. His main research interests include theoretical and practical aspects on model predictive control with application to power electronics, renewable energy integration, and microgrids.



**PABLO POBLETE** (Member, IEEE) was born in Rancagua, Chile. He received the B.Sc. degree with highest honors in electrical engineering from the Pontificia Universidad Católica de Chile, Santiago, in 2018. He is currently working toward the Ph.D. degree in the double-degree Ph.D program between the Pontificia Universidad Católica de Chile, and the University of Technology Sydney.

Since 2017, he has been part of the Power and Energy Conversion Laboratory of the Pontificia Universidad Católica de Chile. His current research interests include power electronics, second-life battery energy storage systems, predictive control, and multilevel converters.



**SEBASTIÁN NEIRA** (Student Member, IEEE) received the B.Sc. (Eng.) degree in electrical engineering from the Pontificia Universidad Católica de Chile, Santiago, Chile, in 2016, and the Ph.D. degree in electrical engineering from Pontificia Universidad Católica de Chile and the University of Edinburgh, Edinburgh, U.K, in 2023.

Since 2017, he has been a member of the Power and Energy Conversion Laboratory, Pontificia Universidad Católica de Chile. Since 2023, he has been a Research Associate in power electronics with the University of Edinburgh, Edinburgh, U.K. His current research interests include the design and control of multiport and multilevel power converters applied to energy storage and solar energy conversion, and industrial applications of SiC MOSFETs.